Monthly Notices of the ROYAL ASTRONOMICAL SOCIETY

MNRAS **529,** 2116–2130 (2024) https://doi.org/10.1093/mnras/stae443
Advance Access publication 2024 February 21

Identifying heavy stellar black holes at cosmological distances with next-generation gravitational-wave observatories

Stephen Fairhurst [1★] Cameron Mills,[2,3] Monica Colpi,[4,5] Raffaella Schneider [6,7,8] Alberto Sesana,[4,5] Alessandro Trinca [7,8] and Rosa Valiante [7,8]

[1]*Gravity Exploration Institute, School of Physics and Astronomy, Cardiff University, Cardiff CF24 3AA, UK*
[2]*Albert-Einstein-Institut, Max-Planck-Institut for Gravitationsphysik, D-30167 Hannover, Germany*
[3]*Leibniz Universitat Hannover, D-30167 Hannover, Germany*
[4]*Department of Physics, University of Milano - Bicocca, Piazza della Scienza 3, I-20126 Milano, Italy*
[5]*National Institute of Nuclear Physics INFN, Milano - Bicocca, Piazza della Scienza 3, I-20126 Milano, Italy*
[6]*Dipartimento di Fisica, Universitá di Roma 'La Sapienza', P.le Aldo Moro 2, I-00185 Roma, Italy*
[7]*INAF-Osservatorio Astronomico di Roma, via di Frascati 33, I-00078 Monteporzio Catone, Italy*
[8]*INFN, Sezione di Roma I, P.le Aldo Moro 2, I-00185 Roma, Italy*

Accepted 2024 February 1. Received 2024 January 24; in original form 2023 November 2

ABSTRACT

We investigate the detectability of single-event coalescing black hole binaries with total mass of 100–600 $M_\odot$ at cosmological distances ($5 \lesssim z \lesssim 20$) with the next generation of terrestrial gravitational wave observatories, specifically Einstein Telescope and Cosmic Explorer. Our ability to observe these binaries is limited by the low-frequency performance of the detectors. Higher order multipoles of the gravitational wave signal are observable in these systems, and detection of such multipoles serves to both extend the mass range over which black hole binaries are observable and improve the recovery of their individual masses and redshift. For high-redshift systems of $\sim 200\,M_\odot$ we will be able to confidently infer that the redshift is at least $z = 12$, and for systems of $\sim 400\,M_\odot$ we can infer a minimum redshift of at least $z = 8$. We discuss the impact that these observations will have in narrowing uncertainties on the existence of the *pair-instability mass gap*, and their implications on the formation of the first stellar black holes that could be *seeds* for the growth of supermassive black holes powering high-z quasars.

Key words: black hole physics – gravitational waves – galaxies: high-redshift.

1 INTRODUCTION

In the three observing runs by the LIGO-Virgo-KAGRA (LVK) Collaboration, many tens of gravitational-wave (GW) transient signals consistent with the merger of binary black holes (BBHs) have been detected (Abbott et al. 2019, 2021a, 2023, 2024; Mehta et al. 2023; Nitz et al. 2023). The systems, observed at $z \lesssim 1$, are found to have component masses between about 6 and 100 $M_\odot$.[1] A variety of channels have been proposed for their origin: formation as field binaries primarily in low-metallicity galaxies at high redshifts, formation in dense stellar systems, in active galactic nucleus discs, or after generations of repeated mergers (see Graziani et al. 2020; Abbott et al. 2021b; Gerosa & Fishbach 2021; Mapelli 2021; Mandel & Farmer 2022, and references therein).

The next-generation of ground-based GW observatories, specifically the Einstein Telescope (ET, Punturo, Lück & Beker 2014; Branchesi et al. 2023) and Cosmic Explorer (CE, Evans et al. 2021), will open the prospect of detecting the GW signatures of merging BBHs over a wider mass range and deeper redshifts, extending the realm of observations to BBHs out to $z \sim 30$, when the first stars began to shine, and into the intermediate-mass range $\mathcal{O}(100\text{–}1000)\,M_\odot$ (Kalogera et al. 2019; Maggiore et al. 2020). Beyond redshift $z \sim 30$–40, merging primordial black holes (BHs) of $\mathcal{O}(10)\,M_\odot$, formed by quantum processes in the early Universe (Carr et al. 2021; Ng et al. 2022), may also be detected and studied (Ng et al. 2022, 2023).

In this paper we study systems with individual masses extending from 60 to 480 $M_\odot$, and total masses of 180 to 600 $M_\odot$, covering a mass range that is relevant for several reasons, as we explore below. Measuring such systems is most interesting at cosmological distances, which is only possible due to the enhanced sensitivity of ET and CE at frequencies below 10 Hz.

The formation of such heavy stellar-mass BHs requires the presence of star-forming regions of zero or extremely low metallicity, where fragmentation and cooling of the parent gas cloud, and mass-loss from stellar winds are strongly suppressed (see Bromm 2013; Spera & Mapelli 2017, and references therein). These are conditions that occur in the high-redshift Universe, and are expected to result in a top-heavy mass function where stars heavier than 150–300 $M_\odot$ are more common than in the conventionally adopted, Kroupa-like, stellar initial mass function (IMF) (see Klessen & Glover 2023 for a recent review on the first stars). At the highest redshifts, these

★ E-mail: FairhurstS@cardiff.ac.uk
[1]All masses in this paper are referred to as measured in the source frame.

heavy BHs may represent systems not yet affected by accretion of gas or stars (Stone, Küpper & Ostriker 2017; Roupas & Kazanas 2019; Safarzadeh & Haiman 2020; van Son et al. 2020), and hence their masses might reflect their birth conditions. Detecting GWs from these heavy stellar-mass binaries will let us constrain their merger rate which is intimately related to the rate of formation of massive stellar binary systems in pristine star-forming galaxies (Stacy & Bromm 2013; Chon & Hosokawa 2019; Mangiagli et al. 2019; Mapelli et al. 2022; Santoliquido et al. 2023; Sugimura et al. 2023).

Some of the BBH masses we investigate reside within the so-called *pair-instability mass gap* [often referred to as upper mass gap or pair instability supernova (PISN) gap]. This gap is between about 65 and 135 $M_\odot$ where no BH is expected to form in evolution models of isolated stars. This mass gap is attributed to a pair instability, arising in metal-poor, massive stars between about 130 and 250 $M_\odot$, which leads to a supernova explosion due to uncontrolled $^{12}C(\alpha, \gamma)^{16}O$ nuclear burning, leaving no remnant (Farmer et al. 2020; Woosley & Heger 2021).

During the third observing run of LVK a short-duration signal, GW190521, was detected and estimated to be consistent with the merger of two BHs with component masses of about 85 and 66 $M_\odot$ and total mass of 142 $M_\odot$ (Abbott et al. 2020b, d). This is the heaviest BH observed in GWs to date, with an *intermediate-mass* remnant and a primary component residing within the *pair-instability mass gap*.[2]

After submission of this paper, new signals have been extracted from the O3 run public LIGO-Virgo data set,[3] hinting for the presence of candidate BBHs with median masses of the primary BHs within the *pair-instability mass gap*, and in one case beyond its upper edge (Wadekar et al. 2023), making even more compelling the analysis on the detectability of these systems.

Detecting the GW signal from high-redshift heavy stellar BBH mergers, where one or both components are in the upper mass gap or straddling it, would be highly informative. Various mechanisms could lead to the formation and coalescence of such binaries, and among them, evolution in isolated binaries (Hijikawa et al. 2021), dynamical encounters, and mergers in star clusters (Rodriguez et al. 2019; Di Carlo et al. 2020a; Kremer et al. 2020), a chain of Nth generation mergers.[4]

Estimates of the location and width of the upper mass gap are at best approximate. Current uncertainties on the reaction rate, on rotation, and on the presence of rich hydrogen envelopes may shift the instability interval for the explosion to higher masses, and narrow further the gap (Belczynski 2020; Farmer et al. 2020; Marchant & Moriya 2020; Vink et al. 2021; Woosley & Heger 2021) or even fill it entirely (Costa et al. 2021). Testing the existence of this upper mass gap and inferring its properties from GW observations depends critically upon the accuracy with which the masses of the individual BHs are measured from the merger signal. Here and for this purpose we carry out a parameter estimation on BBHs with component masses which touch the *edges* of the upper mass gap, recognizing that all of the above arguments become compelling if the redshift of the observed systems is $z \gtrsim 10$.

Determining the *lowest* redshift one can claim the source to be *beyond*, and inferring posteriors for the distribution of the component masses is of paramount importance (Mancarella, Iacovelli & Gerosa 2023). A key challenge, then, is to accurately infer both the masses and redshift of the binary. There is a well-known degeneracy between measurements of the distance to and inclination of a binary from GW observations (Usman, Mills & Fairhurst 2019). At high redshifts, this degeneracy further impacts our ability to infer the masses of the binary. In GW observations, masses and redshift are degenerate, and only the redshifted masses, $m_{1,2}(1+z)$, can be inferred from the signal. Given a cosmological model, the measured distance can be used to obtain the redshift and hence the source masses. However, if the distance is poorly constrained, this leads to significant uncertainties on the mass. For example, it is not unusual to have an uncertainty of ~ 50 per cent in the distance measurement of BBH signals (Abbott et al. 2023). At $z = 10$ this translates to a redshift uncertainty of ± 4 and consequently an uncertainty in the masses of 40 per cent due to redshift effects alone. The ability to accurately infer redshifts and masses is improved by a detector network, which can provide more accurate localization and distance measurements (Fairhurst 2011; Singer et al. 2014; Mills, Tiwari & Fairhurst 2018), as well as the observation of higher order multipoles (HoMs) in the GW signal which help break the distance-inclination degeneracy (Mills & Fairhurst 2021; Fairhurst et al. 2023).

The paper is organized as follows. In Section 2, we discuss the observability of high-mass, high-redshift binaries with a focus on the HoMs. In Section 3, we provide detailed parameter estimation results for a number of astrophysically interesting simulated BBH merger signals and in Section 4 we summarize our results. We include two appendices. Appendix A provides additional figures showing detector sensitivity for binaries of varying mass ratio and Appendix B gives parameter estimation accuracy for low signal-to-noise ratio (SNR) systems.

2 THE IMPORTANCE OF HIGHER ORDER MULTIPOLES

High-mass, high-z BBH coalescences are intrinsically low-frequency GW sources. This is illustrated in Fig. 1, where we show the frequency evolution of the GW strain amplitude for a BBH of (120-60) $M_\odot$ placed at redshift $z = 14$, with an inclination ι of 60° between the orbital angular momentum and the line of sight. The gravitational waveform for this signal only extends to 15 Hz and is therefore outside the sensitive frequency range of current GW observatories. The leading GW emission from the source, emitted in the (2, 2) multipole at twice the orbital frequency, extends to only 7 Hz in the detector, making discovery challenging.[5] Although the (3, 3) and (4, 4) multipoles are intrinsically lower amplitude, they extend to higher frequencies [$\sim$1.5 and 2 times the frequency of the (2, 2)]

[2]Alternative analyses (e.g. Nitz & Capano 2021) find that GW190521 could instead be $\sim 170\,M_\odot$ BH with a companion of $\sim 20\,M_\odot$, suggesting that the primary is already an intermediate-mass BH, with a mass beyond the mass gap (Fishbach & Holz 2020).

[3]The analysis exploits the power of higher order modes, as discussed in this paper.

[4]There are several proposed channels for the origin of the components of GW190521-like systems observed at low redshift. For instance: mergers from the relics of the first stars (known as Population III stars) (Liu & Bromm 2020; Tanikawa et al. 2021), isolated binary evolution with no-gap (Belczynski 2020), stellar collisions in star clusters (see Di Carlo et al. 2020b; Renzo et al. 2020; Arca-Sedda et al. 2021; Costa et al. 2022, and references therein), hierarchical mergers (Gerosa & Fishbach 2021), and finally primordial BBHs (Clesse & García-Bellido 2022).

[5]We recall that for all BBH observed to date, the (2, 2) multipole, which is emitted at twice the orbital frequency, has been the dominant multipole detected in the GW signal. Additional multipoles of the GW signal have been observed for a handful of events (Abbott et al. 2020a, c) but, as their amplitudes are lower, they are generally not identified for the majority of sources.

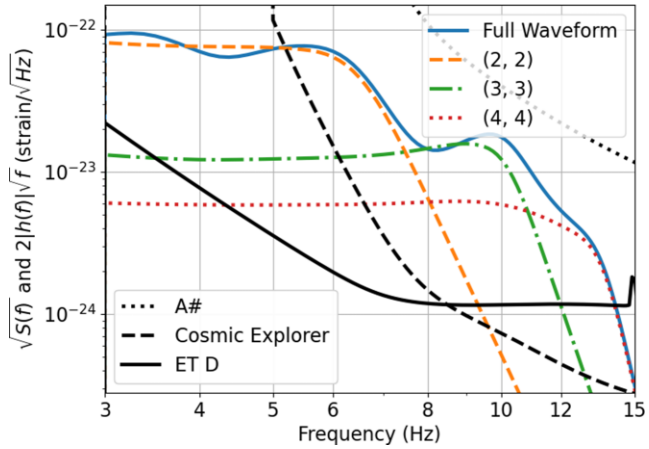

Figure 1. Waveform amplitude from a (120,60) $M_\odot$ binary at $z = 14$, inclined at an angle of 60° to the line of sight. The figure shows the frequency evolution of the waveform, and also the individual contributions from the three leading multipoles (2, 2), (3, 3), and (4, 4) using the IMRPhenomXPHM waveform (Pratten et al. 2021). The oscillations in the full waveform are due to constructive/destructive interference between the multipoles. The projected noise curves for three future detectors: CE, ET, and A# are also shown. The signal is represented in such a way that the area between the wave amplitude and noise is indicative of the SNR (Abbott et al. 2016).

and can therefore contribute significantly to the observed SNR. This improves the prospects of detecting such a system. Furthermore, the identification of these higher order (higher frequency) multipoles in the signal can significantly improve the ability to infer the parameters of the system, as they enable us to break measurement degeneracies that exist with observation of only a single multipole.

There are several well-known degeneracies in the emitted gravitational-waveform, leading to some parameters being very well measured, while others being not. For our purposes, we are most concerned with a degeneracy between the observed distance to and inclination of a binary, as discussed in Usman, Mills & Fairhurst (2019). When only the (2, 2) multipole is observed, the amplitude gives a good measurement of $\cos\iota/d_L$, where ι is the binary inclination and d_L is the luminosity distance. However, in many cases, the binary inclination is only restricted to the range $\iota \in [0°, 60°]$, leading to a factor of 2 uncertainty in distance due to this degeneracy alone. When the binary is observed at a high redshift, the measurement of the masses also becomes degenerate with distance and inclination, and a factor of 2 uncertainty in distance can lead to a similar uncertainty on the masses. The observation of a second GW multipole can serve to break this degeneracy (Abbott et al. 2020a; Mills & Fairhurst 2021) as the relative amplitude of the different multipoles depends upon the orientation of the binary.[6]

In Fig. 2, we show the variation of the SNR with binary mass ratio $q = m_2/m_1$ (assuming an inclination $\iota = 60°$) and inclination (assuming $q = 1/2$) in each of the multipoles for a binary of total mass of 180 $M_\odot$ at $z = 14$ observed by ET. Here, and throughout this section, we use an SNR threshold of 8 for detectability of a signal and an SNR threshold of 3 for observability of a specific multipole, given that the system has an overall SNR above 8. The SNR of the (2, 2) multipole is greatest for face-on signals ($\iota = 0°$) with equal-mass components ($q = 1$). For a face-on signal, the (2, 2) multipole is circularly polarized and, as the inclination increases, the amplitude of both polarizations decreases to a minimum for edge-on systems, $\iota = 90°$, whose emission is linearly polarized. For the other multipoles considered, the SNR vanishes at face-on and peaks at ∼50° for the (3, 3) multipole and ∼60° for the (4, 4) multipole. The binary would be observable in ET at any orientation. For inclinations $\iota \gtrsim 10°$ or 30° the (3, 3) and (4, 4) multipoles would be identifiable, respectively. Since this waveform lasts only a few cycles in the detector band, the contributions from the different multipoles are not orthogonal. Consequently, the total SNR varies with the merger phase of the binary.

The SNR of each different multipole, and the full signal, also varies with mass ratio. The (2, 2) multipole is largest for equal-mass systems and decreases by a factor of 3 by mass ratio $q = 1/5$, while the (3, 3) vanishes for equal mass and peaks around $q = 1/3$. For this signal, the SNR in the (4, 4) multipole does not vary significantly with mass ratio. The (2, 2) and (4, 4) multipoles would be identifiable at any mass ratio, and the (3, 3) for binaries with mass ratio below ∼0.7. Identification of more than one multipole enables an improved measurement of mass ratio, as well as binary orientation.

In Fig. 3, we show the same dependence of SNR with inclination and mass ratio for the CE detector. Since CE has sensitivity to the signal above 5 Hz, rather than 3 Hz for ET, the overall SNR is lower and the signal would be marginally observable. Furthermore, a broad range both in inclination and mass ratio, where the (3,3) multiple gives the dominant contribution to the SNR, becomes accessible. This provides a clear example of a signal where the HoMs enable detection as well as improved parameter recovery.

Given the above discussion, we are interested in identifying the regions of the mass space where HoMs can contribute to either the observability or parameter measurement accuracy of high-mass, high-redshift binaries. In Fig. 4 we show the sensitivity of the proposed ET and CE observatories to BBH mergers with mass ratio of 1:2 as a function of redshift. We show the maximum redshift at which a binary can be observed, at an SNR of 8, and also the redshifts at which 10 per cent, 50 per cent, and 90 per cent of binaries, averaged over sky location and orientation, will be observed. The detector sensitivity is shown for both the (2, 2) multipole, in orange, and the full waveform, in blue. At low masses, the (2, 2) multipole dominates the observable signal and therefore the distance to which the full waveform can be observed is essentially equal to that of the (2, 2) multipole. However, at high masses, the (3, 3) and (4, 4) multipoles contribute more significantly and incorporating them increases the sensitivity of the detectors to these systems. When a system has been observed, the identification of a second multipole, at SNR above 3, can greatly improve parameter recovery by breaking degeneracies between distance and inclination and improving mass ratio measurement. The range of masses and redshifts for which the binary would be observed with SNR above 8, and with SNR above 3 in at least two multipoles, is shown in black in Fig. 4. For example, in ET a 4000 $M_\odot$ system is visible at $z \approx 1$ with the (2, 2) multipole but up to $z \approx 2$ with the full waveform.

Remarkably, for the majority of binaries with $M \gtrsim 100\,M_\odot$ observed by ET, and $M \gtrsim 30\,M_\odot$ observed by CE, a second multipole will be observable. At lower masses, it is the (2, 2) and (3, 3) multipoles which contain most power, while at high masses it is the (3, 3) and (4, 4) multipoles that are observed, with the (2, 2) multipole power occurring at frequencies below the instrumental sensitivity. The picture is similar at different mass ratios, and figures showing the sensitivity to binaries with $q = 1$, 1/2, 1/4, and 1/10 are provided in Appendix A, for ET in Fig. A1 and CE in Fig. A2. The most significant difference occurs for equal-mass binaries, where the (3, 3) multipole vanishes and we therefore require both (2, 2) and (4,

[6]The ratio of the amplitude of the (3, 3) multipole to the (2, 2) scales as $\sin\iota$, while the (4, 4) multipole scales as $\sin^2\iota$ relative to the (2, 2).

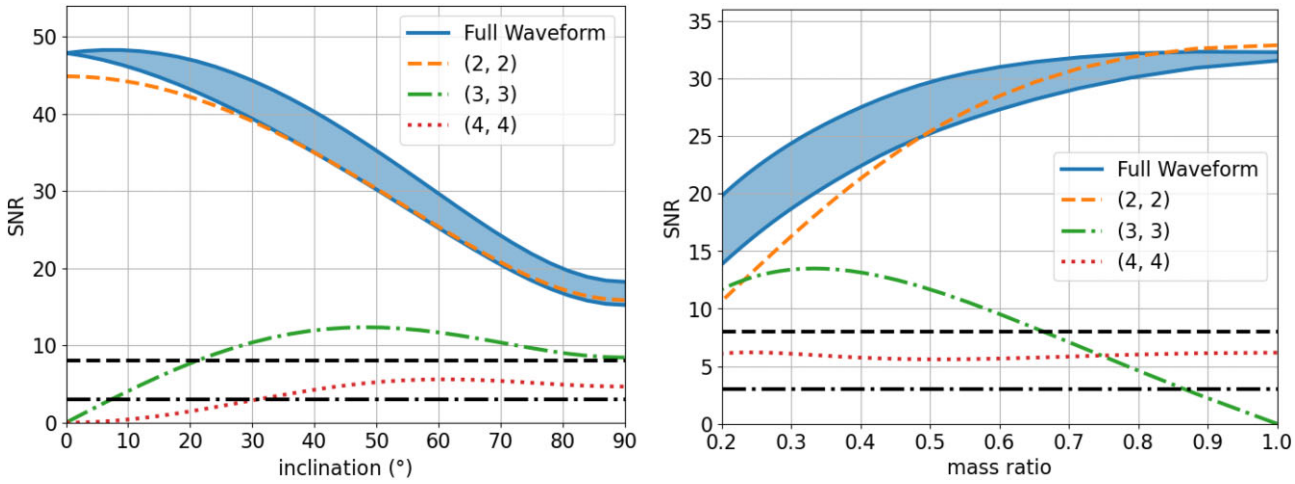

Figure 2. The total SNR and SNR in each multipole in ET for a binary of total mass of 180 $M_\odot$, at redshift $z = 14$ and overhead the detector. Left: variation of SNR with inclination of the binary, for a BBH of (120, 60) $M_\odot$ and the fixed redshift. Right: variation of SNR with mass ratio, for a 180 $M_\odot$ binary with inclination of 60° at the fixed ratio. The total SNR for the system is computed using the (2, 2), (2, 1), (3, 3), (3, 2), and (4, 4) multipoles and individual SNRs for the (2, 2), (3, 3), and (4, 4) multipoles are shown. At $\iota = 0$ in the left panel the full waveform SNR is higher than the (2,2) mode due to the contribution of the (2, 1) and (3, 2) modes, which are not shown. The total SNR depends upon the phase of the signal at merger, due to non-zero overlap between multipoles, and is therefore shown as a shaded blue area. In both panels, the horizontal lines indicate SNR = 8, an approximate threshold for detection, and SNR = 3, an approximate threshold for observation of a second multipole, given that another multipole has been observed (Mills & Fairhurst 2021).

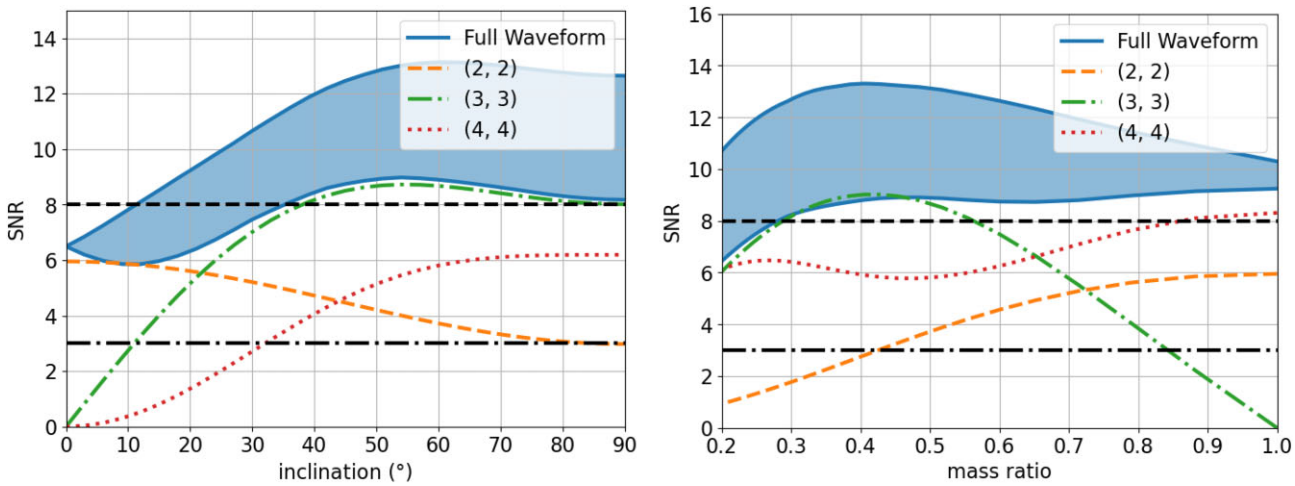

Figure 3. The same as Fig. 2 but for CE.

4) multipoles to be observable. This limits the range for which two multipoles can be seen and increases the minimum mass at which we expect to observe two multipoles to $\sim 200\,M_\odot$ in ET and $\sim 50\,M_\odot$ for CE. None the less, for the majority of high-mass, high-redshift binaries, we expect to observe multipole multipoles, and therefore obtain good estimates of both the masses and redshift of the system. In the next section, we investigate those expectations in detail through parameter recovery of a series of systems.

3 PARAMETER RECOVERY FOR HIGH-MASS, HIGH-REDSHIFT BINARIES

Observation in a single GW observatory leads to large uncertainties in the sky location of the binary (Singer et al. 2014), and this is again degenerate with the inferred distance and redshift. A network of detectors with comparable sensitivity can provide accurate localization (Mills, Tiwari & Fairhurst 2018) and therefore improved redshift and mass accuracy. Binaries with BH spins misaligned with the orbital angular momentum will precess. In principle, the observation of precession can further improve parameter estimates. However, given that so few cycles of the waveform are visible in the detectors, the prospects for observing precession are slim (Green et al. 2021). Therefore, in what follows we neglect precession effects.

To illustrate the expected performance of a next-generation GW network in observing and measuring these binaries, we perform a number of simulations and obtain parameter estimates with the LALInference (Veitch et al. 2015) package and a uniform in comoving volume distance prior. We simulate four different binary mass combinations, denoting (in the source frame) with m_1 (m_2) the primary (secondary) mass and with M the total mass. We consider (120, 60) $M_\odot$ and (90, 90) $M_\odot$ binaries, chosen so that component BHs lie in, or close to the upper mass gap, and (240, 120) $M_\odot$ and (480, 120) $M_\odot$ binaries chosen to probe observability of high-

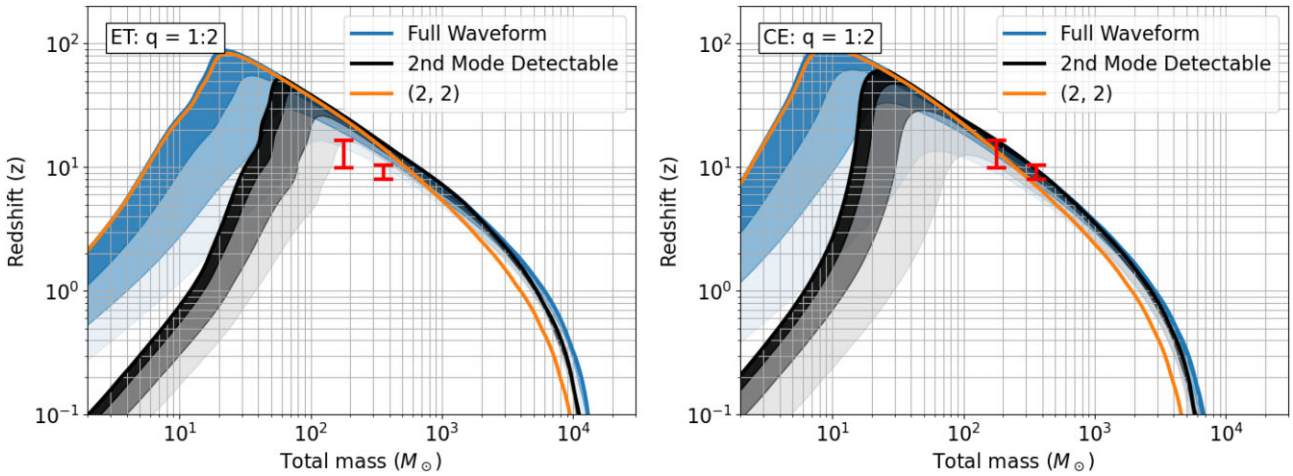

Figure 4. Maximum observable redshift of binaries with mass ratio $q = 1/2$ with next-generation observatories. Left: ET, Right: CE. The shaded regions show redshifts at which 10 per cent, 50 per cent, and 90 per cent of sources are observable. The maximum observable redshift of the (2, 2) multipole at SNR = 8 is shown in orange, the observability of the full waveform at SNR = 8 is shown in blue, and the observability of the second most significant multipole above SNR = 3 is shown in black. The red bars mark the masses and range of redshifts of the $q = 1/2$ systems we study in detail in Section 3.

redshift intermediate-mass black hole (IMBH) in binaries.[7] In all cases, we simulate quasi-circular non-spinning BBHs, but allow for non-zero, aligned spins when performing parameter estimation.[8] This is important as the degeneracy between the binary mass ratio and BH spins (Hannam et al. 2013; Fairhurst et al. 2023) greatly impacts the accuracy with which mass ratio can be measured.

The simulated signals are added to data from a three-detector network of observatories with sensitivity matching ET (Punturo, Lück & Beker 2014) and CE (Evans et al. 2021). Specifically, we use a single, triangular ET detector located in Europe and two 40 km CE observatories, one in the USA and one in India. The simulations are performed at the optimal sky location for the network. Given the greater low-frequency sensitivity of ET, this leads to the binaries being essentially overhead ET. The signals are generated at varying inclination angle, to enable us to investigate the importance of HoMs. We choose the redshift of the sources to ensure a fixed SNR for all signals. In the main text, we use an SNR of 30, while in Appendix B we investigate quieter signals with an SNR of 15.

3.1 Observing mass-gap objects

A mass gap in the BH mass distribution is expected due to the presence of the PISN. Farmer et al. (2020) investigated the location of this pair-instability region as a function of the temperature-dependent uncertainty in the $^{12}C(\alpha, \gamma)^{16}O$ reaction rate. Determining the value of the $^{12}C(\alpha, \gamma)^{16}O$ reaction rate is extremely important for tracing the evolution of massive stars. Thus, restricting this rate through GW observations would be of considerable astrophysical interest. According to Farmer et al. (2020), the width of the mass gap remains roughly constant as a function of the (unknown) reaction rate, but the mass range where no BH can form varies. At the lowest rate relative to the median, the mass gap extends from ~ 90 to $\sim 175\,M_\odot$. At the highest rate, the location of the mass gap is between ~ 60 and $\sim 120\,M_\odot$. Interestingly, there exists a region of BH masses between 90 and $120\,M_\odot$ where we should not expect any BH to form, *for any rate*. We refer to this region as the *forbidden strip*. Consequently, we choose to investigate systems which host at least one member with mass touching this narrow strip. Then, if their masses were to be determined with sufficient accuracy, their detection could constrain the $^{12}C(\alpha, \gamma)^{16}O$ reaction rate to be at the extreme of the allowed range (see fig. 5 of Farmer et al. 2020). In particular, we focus on $(120, 60)\,M_\odot$ and $(90, 90)\,M_\odot$ binaries which have components at the lower and upper range of the forbidden strip.

As seen in Fig. 4, BBHs with masses $(120, 60)\,M_\odot$ will be detectable at a maximum redshift of $z \sim 25$, for an optimally located and oriented system, with 50 per cent of mergers at $z \sim 17$ and the vast majority of events at $z \sim 10$ being detectable. The sensitivity to $(90, 90)\,M_\odot$ systems is comparable. If $(90, 90)\,M_\odot$ systems were to be observed, this will allow us to constrain the strength of the uncertain $^{12}C(\alpha, \gamma)^{16}O$ reaction rate. In particular, BHs with such masses would imply the rate to be at the lower end of the explored range. A binary with mass $(120, 60)\,M_\odot$ would be challenging to form through stellar evolution. Specifically, allowing for variation in the reaction rate, the mass of the primary would require a very high reaction rate for $^{12}C(\alpha, \gamma)^{16}O$, while the mass of the secondary would be compatible with a value below the median. Therefore, this would be a system where only one of the two BHs could originate from stellar evolution and the other would require a different formation channel.

In Figs 5 and 6, we show the recovered parameter accuracies for both mass and redshift for $(90, 90)\,M_\odot$ and $(120, 60)\,M_\odot$ binaries observed with SNR = 30. The first thing to note is that these high-mass, high-redshift systems could be identified with good accuracy by the next-generation GW network, as would be expected due to the relatively large SNRs. For all events, there is, at most, a factor of 2 uncertainty in the mass of the systems and a 50 per cent uncertainty in the redshift, with both numbers quoted at the 90 per cent confidence interval. However, we also notice a substantial variation in the accuracy of parameter measurement between the systems. The parameters of systems close to face-on ($\iota = 0^\circ$ or 30°) are recovered with significantly larger uncertainties than those which are more

[7]IMBH are BHs in the nominal (but loosely defined) range between about $100\,M_\odot$ and about $10^5\,M_\odot$.
[8]The restriction to non-spinning BBH is solely to simplify presentation – all results presented here could be easily extended to aligned-spin BHs.

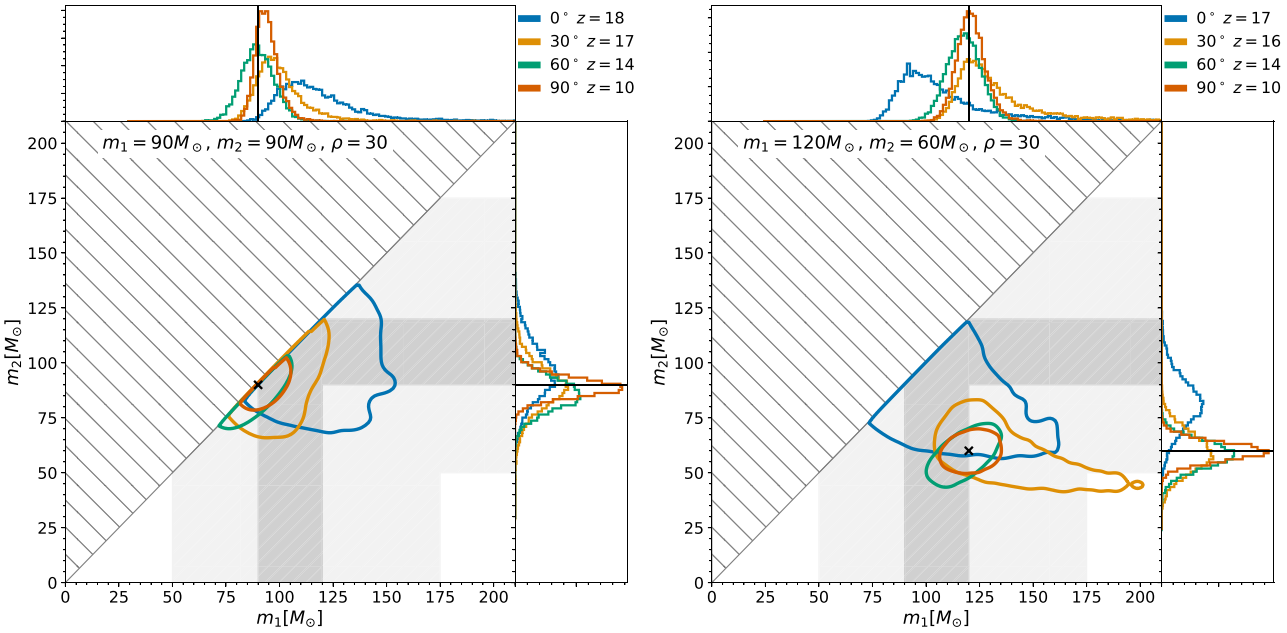

Figure 5. Inferred posteriors of component masses for binaries of total mass of 180 $M_\odot$ which have components at the lower and upper range of the forbidden strip. Results are shown for inclinations of $\iota = 0°$, 30°, 60°, and 90°, with the redshift of the system varied, as indicated in the labels, so that the signals are all simulated with an SNR of 30 in the ET–CE network, at the most sensitive sky location for the network. The grey region denotes the pair-instability mass gap and the darker grey denotes the forbidden strip where no BH is expected to form for any value of the $^{12}C(\alpha, \gamma)^{16}O$ reaction rate (Farmer et al. 2020). Simulated values are denoted by a black cross and contours show the 90 per cent credible region. Left: Binary with masses just below the mass gap: $m_1 = m_2 = 90\,M_\odot$. Right: Binary with masses that straddle the mass gap: $m_1 = 120\,M_\odot$ and $m_2 = 60\,M_\odot$. Greek letter ρ indicates the SNR, throughout the paper.

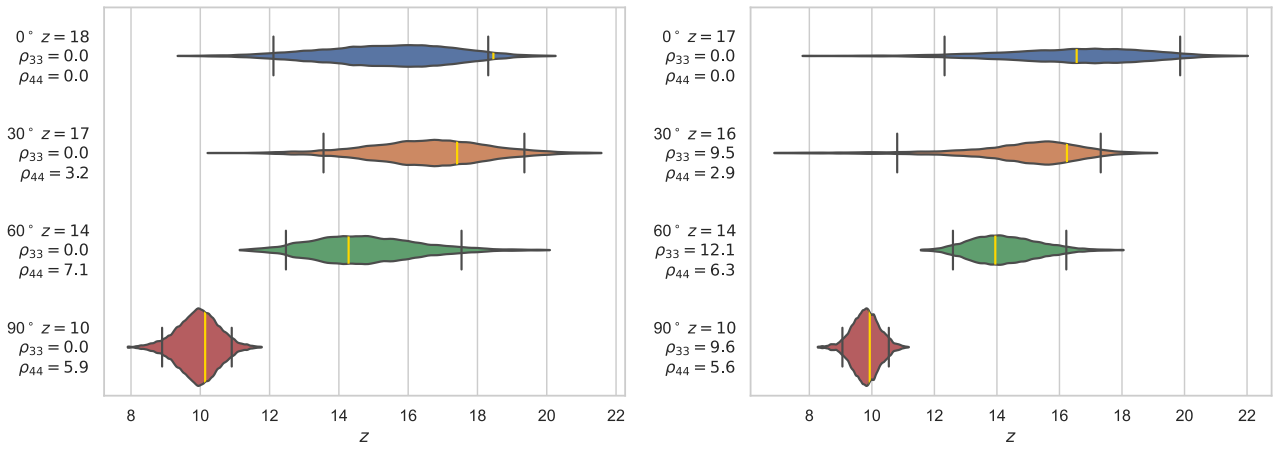

Figure 6. Inferred posteriors for the redshift for binaries of total mass of 180 $M_\odot$ which have components at the lower and upper range of the forbidden strip. Signals are simulated with varying inclination (in degrees) and redshift (z), as indicated in the labels, with a fixed SNR of 30 in the ET–CE network, at the most sensitive sky location for the network. Symbols $\rho_{\ell m}$ indicate the SNR in the (ℓ, m) multipole HoMs. The black vertical lines indicate the 90 per cent credible intervals, violins show the 99.5 per cent range, and the yellow vertical lines show simulated values. Left: binary with masses just below the mass gap: $m_1 = m_2 = 90\,M_\odot$. Right: binary with masses that straddle the mass gap: $m_1 = 120\,M_\odot$ and $m_2 = 60\,M_\odot$.

highly inclined ($\iota = 60°$ or 90°). When the binary is close to face-on, the uncertainty in the component mass posterior is much greater and, for $\iota = 0°$, the 90 per cent mass region for the (120, 60) $M_\odot$ binary includes equal masses. As the inclination of the binary is increased, parameter accuracy improves significantly: already at $\iota = 30°$ the posterior for the (120, 60) $M_\odot$ binary is inconsistent with equal masses, although large uncertainty in the mass ratio remains. For binaries inclined at 60° or 90° the parameter accuracy is excellent. In both cases, the mass ratio is very well constrained and uncertainty in total mass and redshift is ±(10–20) per cent.

We can explain *why* the results of our parameter accuracy display the features they do, using our understanding of the importance of HoMs discussed in Section 2. Let us begin by considering the (120, 60) $M_\odot$ system at $z = 14$, inclined at $\iota = 60°$, that we have plotted in Figs 1, 2, and 3. The signal is observed with high SNR in ET and the (3, 3) multipole is also clearly observed. In CE, the total SNR of the system is sufficient for it to be observed, with the

(3, 3) multipole providing the dominant contribution. Since the event is observed in three detectors, it is relatively well localized,[9] with a 90 per cent localization area of 300 deg^2. The observation of HoMs in the waveform enables the accurate inference of both the binary inclination and mass ratio. Since the sky location, mass ratio, and inclination are well measured, this enables accurate inference of the distance to the binary and consequently the redshift of the source. In the top panel of Fig. 7 we show the recovered values for the redshift, binary inclination, and mass ratio. All three are recovered with an accuracy better than 10 per cent.

Next, we consider a comparable system observed face-on ($\iota = 0^\circ$) at the same SNR, and at a redshift of 17. In that case, the power in both the (3, 3) and (4, 4) multipoles vanishes. Consequently, the binary is no longer observable in CE as it has an SNR of 1.[10] At this SNR, the CE observatories are unable to provide localization of the source, with a 90 per cent localization area of 10 000 deg^2. Furthermore, the vanishing HoMs means that only the (2, 2) multipole is observed in ET. Therefore, it is not possible to break the degeneracy between binary orientation and distance, nor to place a tight constraint upon the mass ratio. The bottom panel of Fig. 7 shows the recovered redshift, mass ratio, and inclination for this system. The mass ratio *is not* accurately recovered and, indeed, the binary is inferred most likely be (close-to) equal mass, although the distribution does extend to $q = 1/2$. In addition, the binary orientation is not accurately recovered, with a broad distribution of $\iota \lesssim 25^\circ$ – more inclined systems are excluded as they would have observable power in the (4, 4) multipole. The mass ratio–inclination distribution does show a secondary peak close to the simulated value ($q \approx 1/2$ and $\iota < 10^\circ$); however, the preference is for an equal-mass system. Despite both mass ratio and inclination being offset from the true values, the inferred redshift matches well with the simulated value. However, due to the uncertainties in other parameters, the redshift uncertainty is now close to 25 per cent. The comparison of parameter accuracy for these two systems highlights the importance of both a network of detectors and also observability of the HoMs in accurate inference of binary properties.

It is worth noting that our intuition from current GW observations that the majority of sources are close to face-on (or face-off) no longer holds in the next-generation network (Vitale 2016). In the nearby Universe, where sources are approximately uniform in volume, a signal observed with a given SNR is most likely to originate from a distant binary which is close to face-on (or face off) as the number of sources increases as d_L^2. For a high-redshift source, whose redshift is past the peak of the redshift distribution – likely around a redshift of $z \approx 2$ at which star formation peaks – this is no longer the case. Now, the most likely origin is from a binary which is at lower redshift, where the intrinsic rate is higher, and is either poorly oriented or from a region of the sky where the detectors have lower sensitivity. Thus, the results from sources inclined at 60° and 90° are more typical of the observed population.

Let us return to the implications for probing the location of the PISN mass gap. For both mass pairs, binaries inclined at 60° or 90° are those which provide the best mass measurements. For the

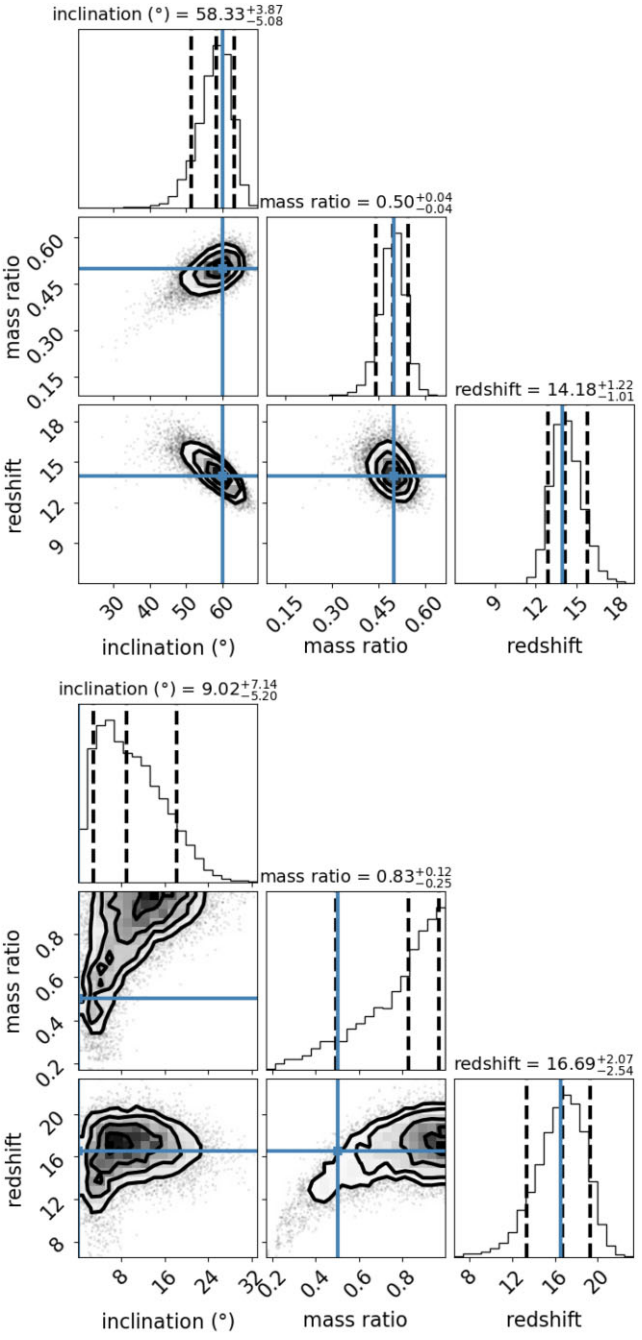

Figure 7. Inferred posteriors for redshift, mass ratio ($q = m_2/m_1$), and inclination for (120, 60) $M_\odot$ binary observed at SNR=30. Top: parameter recovery for a system at $z = 14$ and $\iota = 60^\circ$. Bottom: parameter recovery for a system at $z = 17$ and $\iota = 0^\circ$.

(90, 90) $M_\odot$ system, we have m_1 and m_2 measured in the interval $\in [70, 100]\,M_\odot$. So, this system is consistent with both components lying below the mass gap provided the $^{12}C(\alpha, \gamma)^{16}O$ rate is low. For the (120, 60) $M_\odot$ system, we have $m_1 \in [100, 140]\,M_\odot$ and $m_2 \in [40, 80]\,M_\odot$. The masses are consistent with one above and one below the gap, provided the reaction rate is high. If *both* signals were observed, this would be inconsistent with our current understanding of the PISN mass gap.

To investigate the observability at even higher redshifts, we have simulated a second set of signals, with the same masses and inclina-

[9]Since these are very low-frequency systems, the localization is poorer than for events in GWTC-3 (Abbott et al. 2023) as the localization depends upon the frequency bandwidth of the signal (Fairhurst 2009).

[10]The waveform shown in Fig. 3 corresponds to a binary at $z = 14$ and we are now considering the same mass binary at $z = 17$. The larger redshift reduces the SNR primarily through redshifting the signal which lowers the frequency by 20 per cent. This leads to an SNR which is lower than that shown in the figure.

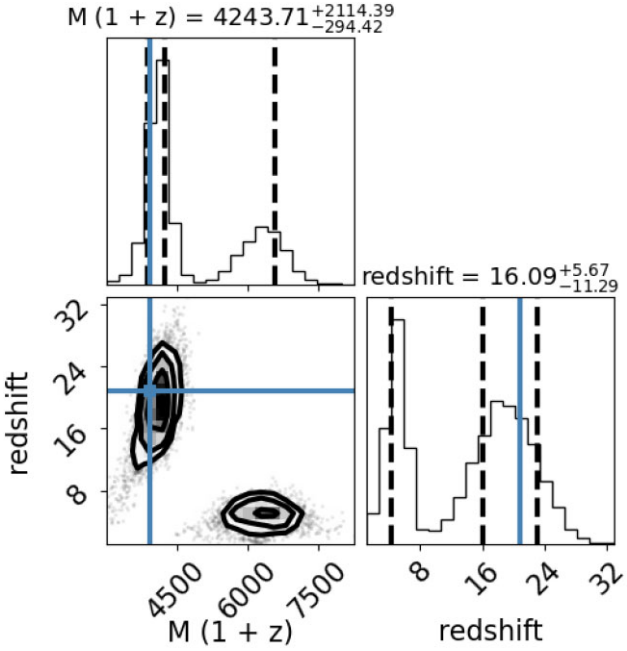

Figure 8. Inferred posteriors for redshift and redshifted mass for a simulated (120, 60) $M_\odot$ BBH merger with $\iota = 0^\circ$ observed at $z = 21$.

tions but with a lower SNR fixed at 15. For these systems, the redshifts range from $z \gtrsim 20$ for face-on systems to $z \approx 15$ for edge on systems. Broadly, the results are consistent with those in Figs 5 and 6, but with larger uncertainties due to the lower signal amplitude. In particular, for all but the face-on systems, we are able to clearly identify that the (120, 60) $M_\odot$ binary is of unequal mass, due to the observed power in HoMs. For the inclined systems, the uncertainty in total mass and redshift is around a factor of 2 (from 150 to 300 $M_\odot$ and $z = 12$ to 25). Thus, while it is possible to identify these systems as unambiguously high-mass and high-redshift sources, the uncertainties in masses and redshifts make it difficult to perform precision astrophysics. For the (90, 90) $M_\odot$ system, it is only at $\iota = 60^\circ$ or 90° that the parameters are well recovered. These results are shown in Figs B1 and B2 in Appendix B.

For the face-on systems, we see an interesting feature whereby the binary can be mistaken for a different system with very different properties. Fig. 8 shows the inferred redshift and redshifted mass – $M(1 + z)$ – distributions for a (120, 60) $M_\odot$ system at $z = 21$. The primary peak is at $z = 21$ and $M(1 + z) \approx 4,000\,M_\odot$ corresponding to the simulated value. However, there is a secondary peak around $z = 5$, with a redshifted mass around 6000 $M_\odot$ corresponding to a binary with mass of 1000 $M_\odot$. For this system, it is the (3, 3) multipole which is consistent with the simulated signal. This provides another example of the challenges which arise when identifying high-mass, high-redshift binaries. The signal would be observed only in ET, and have only one observable multipole. Not only does this lead to poor parameter recovery, but also the inability to distinguish between a 180 $M_\odot$ binary at $z = 21$ and a 1000 $M_\odot$ binary at $z = 5$. Given the GW data alone, it would not be possible to distinguish between the two scenarios. The relative significance of the two will depend upon astrophysical knowledge of the mass and redshift distributions of BBHs. Here, we have used priors which are uniform in comoving volume and component masses. Other choices might lead to different conclusions about the mass and redshift of the binary.

In summary, for these two representative sources, and for high SNRs we would confidently identify the systems as high-mass BBHs at high redshift. These could be potential seeds for the growth of supermassive BHs. The first system of (90, 90) $M_\odot$ would be marginally consistent with being a binary formed at the lower edge of the mass gap, in correspondence of the lowest value of the $^{12}C(\alpha, \gamma)^{16}O$ reaction rate, and inconsistent otherwise. The second system of (120, 60) $M_\odot$ would be consistent with one BH (the lightest) originating from the core-collapse of a massive star (provided the $^{12}C(\alpha, \gamma)^{16}O$ rate is low) and the second, in the midst of the pair-instability gap, would have a different origin. For a large fraction of the computed rates, the discovery of the latter system would be inconsistent with the explosion scenario implied by the pair instability that would predict no BHs, and therefore a different channel has to be called for, for both components.

3.2 Observing IMBHs in binaries jumping the gap

In this section and for concreteness, we consider binaries with masses (240, 120) $M_\odot$ and (480, 120) $M_\odot$ which would be observable up to $z \sim 10$, and explore their detectability. While the 120 $M_\odot$ BH would be at the border of the pair-instability gap, both primary BHs are well above the gap.

The formation of such massive stellar BH would either require, in the isolated channel, a Kroupa-like IMF extending from solar to at least 500 $M_\odot$, or a top-heavy IMF. Alternatively, they may have formed through runaway stellar collisions or hierarchical BH mergers in dense, pristine star cluster, by fast accretion, or be the result of rotating collapsing massive stars or clouds as in the direct scenario for BH seed formation (see Volonteri, Habouzit & Colpi 2021, for a review). Their formation in binaries is uncertain so that their detection would be extremely valuable. Thus, for these systems we are interested in determining whether the mass of the primary and the redshift can be accurately inferred in order to identify them as early IMBHs.

Figs 9 and 10 show the accuracy with which we can measure the masses and redshifts of the events. The broad features are similar to what we have already observed for the lower mass systems, namely that the parameter recovery is significantly worse for face-on systems, due to the vanishing HoMs. Even though the mass ratio of the systems is 2 or 4, both are inferred to be consistent with equal-mass (or nearly equal mass) binaries when viewed face-on. Furthermore, the uncertainty in redshift and total mass is about a factor of 2. For the inclined systems, the recovery of masses and redshifts improves significantly, particularly for $\iota \geq 60^\circ$. In that case, component masses and redshifts are recovered with a ~ 20 per cent accuracy. In particular, the mass of the 120 $M_\odot$ BH will be constrained to be between 90 and $\sim 150\,M_\odot$ for all except for the face-on system. This is consistent with a BH above the mass gap and, due to uncertainties in the mass measurement, will not significantly restrict the $^{12}C(\alpha, \gamma)^{16}O$ reaction rate. In Appendix B, we also show results for events simulated at higher redshifts and at a lower SNR of 15. The results are comparable to those discussed above, with the masses and redshifts for inclined systems better measured, and masses constrained to be unequal. For face-on systems, the parameter recovery is significantly worse and we again see multiple peaks in the mass–redshift distributions corresponding to different multipoles matching with the signal.

Remarkably, the next-generation GW observatories have the capability to detect and accurately identify mergers involving 240 $M_\odot$ BH at a redshift of 10, and confidently infer a minimum redshift of 7, and mergers involving a 480 $M_\odot$ BH at a redshift of 6, and infer

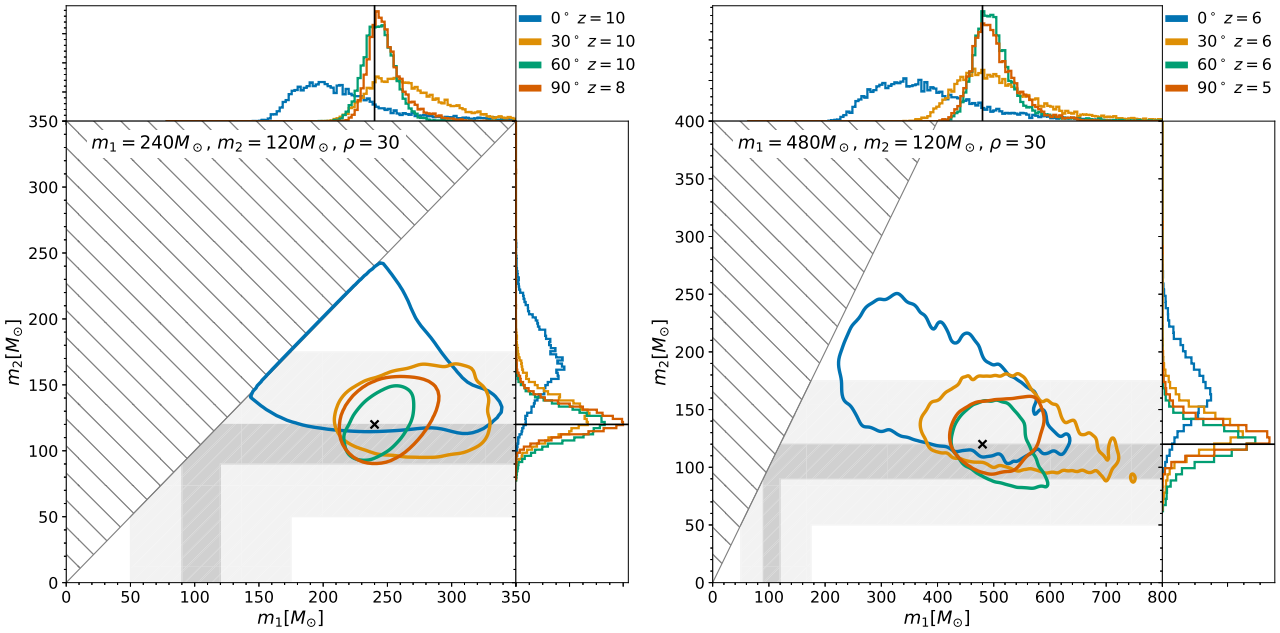

Figure 9. Inferred posteriors for the component masses for heavy binaries. Results are shown for inclinations of $\iota = 0°$, $30°$, $60°$, and $90°$, with the redshift of the system varied, as indicated in the labels, so that the signals are all simulated with an SNR of 30 in the ET–CE network, at the most sensitive sky location for the network. The grey region denotes the pair-instability mass gap and the darker grey denotes the forbidden strip where no BH is expected to form for any value of the $^{12}C(\alpha, \gamma)^{16}O$ reaction rate (Farmer et al. 2020). Simulated values are denoted by a black cross and contours show the 90 per cent credible region. Left: $m_1 = 240\,M_\odot$ and $m_2 = 120\,M_\odot$. Right: $m_1 = 480\,M_\odot$ and $m_2 = 120\,M_\odot$.

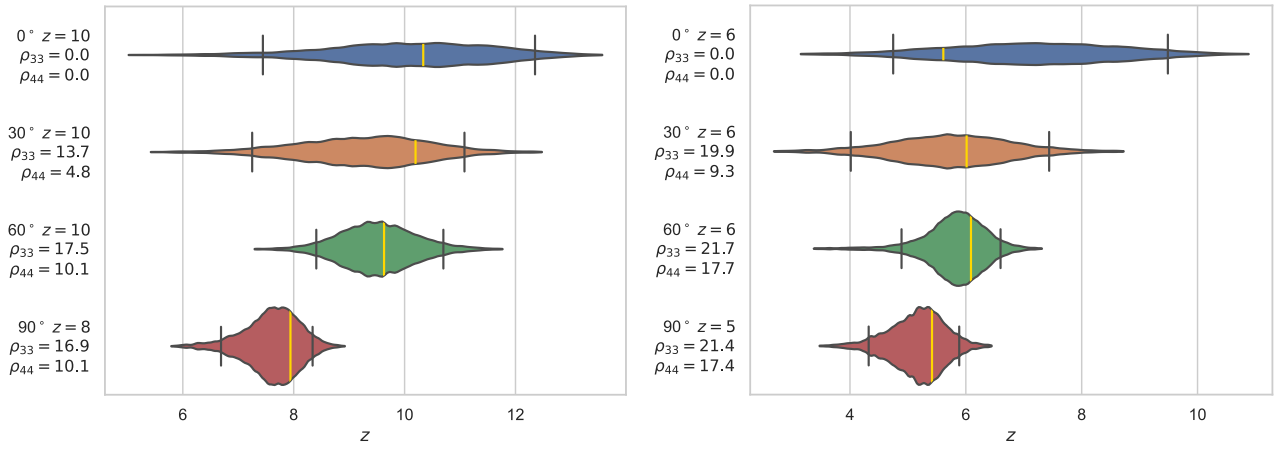

Figure 10. Inferred posteriors for the redshift for heavy binaries. Signals are simulated with varying inclination and redshift, as indicated in the labels, with a fixed SNR of 30 in the ET–CE network, at the most sensitive sky location for the network. The black vertical lines indicate the 90 per cent credible intervals, violins show the 99.5 per cent range, and the yellow vertical lines show simulated values. Symbols $\rho_{\ell m}$ indicate the SNR in the (ℓ, m) multipole HoMs. Left: $m_1 = 240\,M_\odot$ and $m_2 = 120\,M_\odot$. Right: $m_1 = 480\,M_\odot$ and $m_2 = 120\,M_\odot$.

a redshift of at least 4. These systems will be interesting to observe because we do not know if BHs of those masses exist, and we can hope to shed light on their formation routes, either by accretion from lower mass BHs or by direct collapse of very massive stars.

4 DISCUSSION

The next-generation of terrestrial GW observatories will have the sensitivity to identify signals from heavy stellar BHs with masses straddling the upper mass gap, or even jumping it, up to masses as high as $\sim 500\,M_\odot$, out to $z \sim 10$–15. The discovery of these systems may constrain some of the formation processes and possibly the shape and extension of the IMF, by reducing degeneracies.

If BHs in the mass range explored in this study do exist, they can contribute, as *seeds*,[11] to the rapid growth of the population of quasars observed close to the recombination epoch, at $z \approx 7.5$, and housing accreting BHs of $\mathcal{O}(10^8$–$10^9)\,M_\odot$ (e.g. Volonteri & Rees 2005; Madau, Haardt & Dotti 2014; Pezzulli, Valiante & Schneider 2016; Volonteri, Silk & Dubus 2015; Ricarte & Natarajan 2018;

[11]The so-called 'light seeds' explored in the literature (Valiante et al. 2017; Inayoshi, Visbal & Haiman 2020; Volonteri, Habouzit & Colpi 2021).

Valiante et al. 2021; Trinca et al. 2023). Whether and how the bridge between stellar and supermassive BHs was established is currently unknown (Volonteri, Habouzit & Colpi 2021).

The recent discovery by *JWST* of more than 40 new faint accreting supermassive BHs of $\mathcal{O}(10^5$–$10^7\,M_\odot)$ at $4 < z \leq 10.6$ (see Maiolino et al. 2023, and references therein) starts shedding light on the way supermassive BHs form and grow in the Universe (Schneider et al. 2023). In the future, with the Laser Interferometer Space Antenna in operation (Amaro-Seoane et al. 2017), we will detect low-frequency GWs from merging massive BHs of $\mathcal{O}(10^4$–$10^6\,M_\odot)$ out to $z \sim 10$–15. By combining and confronting statistically the electromagnetic and GW observations of accreting and merging BHs from the present out to $z \sim 10$–15, we hope to shed light on the origin(s) and evolution of BHs, from the stellar to the supermassive through the intermediate-mass ones and whether a link exists among these populations (Valiante et al. 2021; Fragione & Loeb 2023).

In this paper, we focused on the observability of high-redshift stellar BBHs with high masses, and, equally importantly, on the accuracy with which their masses and redshifts can be inferred. We have shown that both the observation of systems and the accurate measurement of their parameters depend critically on the inclusion of HoMs in the GW waveform. At the highest masses and redshifts, HoMs, which extend the signal to higher frequencies than the (2, 2) multipole, can significantly increase the sensitive range of the detectors. Across a broad range of masses and redshifts, we expect to see GW multipoles in signals observed by CE and ET. Observation of more than one multipole, typically an HoM in addition to the (2, 2) multipole, enables the breaking of the degeneracy between binary inclination and distance, as well as a more accurate determination of the mass ratio. Additionally, a network of observatories is required for source's localizations. When a signal is seen in only a single detector, the sky location is poorly measured and, since the detector response varies significantly over the sky, this leads to large uncertainties in the distance. For very high-redshift sources, accurate distance/redshift measurement is vital for the measurement of the BH individual masses, as the observed signal depends upon $M(1 + z)$. By performing full parameter estimation on a set of representative systems, we demonstrated that it will be possible to measure masses and redshifts with an accuracy of 10–20 per cent, for signals at redshifts up to at least 15. Those systems which can be observed and accurately measured are typically seen in both CE and ET detectors, so they are well localized and also tend to be viewed away from face-on (or face-off) so that more than one GW multipole is observed.

We examined systems with masses $(120, 60)\,M_\odot$ and $(90, 90)\,M_\odot$, which lie in, or around, the *pair-instability mass gap*. For the best-measured examples we investigated, at a redshift of 10, we could measure redshift and component masses with 10 per cent uncertainly. This would, unambiguously, place these sources in the high-redshift Universe and serve to constrain the, currently unknown, location of the *pair-instability mass gap*. We also investigated mergers of $(240, 120)\,M_\odot$ and $(480, 120)\,M_\odot$ binaries, which enable us to probe the observability of early IMBH. It will be possible to observe these IMBH at redshifts up to $z = 10$ and constrain the redshift to be at least $z = 7$.

The results in this paper complement those in Ng et al. (2022, 2023) which investigate lower mass BH mergers in the next-generation GW network, and Mancarella, Iacovelli & Gerosa (2023) who introduced the concept of an 'inference horizon' which maps the redshift a source can confidently be placed beyond. In all cases, it is shown that next-generation GW network provides a unique capability to probe high-redshift BH formation.

The most critical feature of detector sensitivity for observing these systems is the low-frequency sensitivity of the detectors. In our study, we used a low-frequency limit of 3 Hz for ET and 5 Hz for CE. Even the relatively small change from 3 to 5 Hz can have a profound impact on sensitivity to high-mass, high-redshift sources as shown in Figs 2 and 3. Achieving the instrumental design sensitivity at low frequencies has been challenging in the current LIGO and Virgo observatories. As the detailed technical designs of the next-generation observatories are finalized, the desire to probe the remnants of high-mass stars in the early Universe should be considered as a motivation to optimize sensitivity at low frequencies.

ACKNOWLEDGEMENTS

We thank Riccardo Buscicchio for his careful reading and valuable comments. SF acknowledges the support of STFC grant ST/V005618/1 and a Leverhulme Trust International Fellowship. RS acknowledges support from the Amaldi Research Centre funded by the MIUR programme 'Dipartimento di Eccellenza' (CUP:B81I18001170001). MC, RS, AT, and RV acknowledge the INFN TEONGRAV specific initiative. MC acknowledges support by the 2017-NAZ- 0418/PER grant, and by the Italian Ministry for Universities and Research (MUR) program 'Dipartimenti di Eccellenza 2023-2027', within the framework of the activities of the 'Centro Bicocca di Cosmologia Quantitativa (BiCoQ)'. AS acknowledges the financial support provided under the European Union's H2020 ERC Consolidator Grant 'Binary Massive Black Hole Astrophysics' (B Massive, Grant Agreement: 818691). MC and RS thank the Institut d'Astrophysique de Paris for kind hospitality.

DATA AVAILABILITY

The simulated data underlying this article are available in a Zenodo repository, at https://dx.doi.org/10.5281/zenodo.10729085. Code for reproducing figures in the paper is available at https://github.com/sfairhur/BBHseeds_hm.

REFERENCES

Abbott B. P. et al., 2016, Phys. Rev. X, 6, 041015
Abbott B. P. et al., 2019, Phys. Rev. X, 9, 031040
Abbott R. et al., 2020a, Phys. Rev. D, 102, 043015
Abbott R. et al., 2020b, Phys. Rev. Lett., 125, 101102
Abbott R. et al., 2020c, ApJ, 896, L44
Abbott R. et al., 2020d, ApJ, 900, L13
Abbott R. et al., 2021a, Phys. Rev. X, 11, 021053
Abbott R. et al., 2021b, ApJ, 913, L7
Abbott R. et al., 2023, Phys. Rev. X, 13, 041039
Abbott R. et al., 2024, Phys. Rev. D, 109, 022001
Amaro-Seoane P. et al., 2017, preprint (arXiv:1702.00786)
Arca-Sedda M., Rizzuto F. P., Naab T., Ostriker J., Giersz M., Spurzem R., 2021, ApJ, 920, 128
Belczynski K., 2020, ApJ, 905, L15
Branchesi M. et al., 2023, J. Cosmol. Astropart. Phys., 2023, 068
Bromm V., 2013, Rep. Prog. Phys., 76, 112901
Carr B., Kohri K., Sendouda Y., Yokoyama J., 2021, Rep. Prog. Phys., 84, 116902
Chon S., Hosokawa T., 2019, MNRAS, 488, 2658
Clesse S., García-Bellido J., 2022, Phys. Dark Universe, 38, 101111
Costa G., Bressan A., Mapelli M., Marigo P., Iorio G., Spera M., 2021, MNRAS, 501, 4514
Costa G., Ballone A., Mapelli M., Bressan A., 2022, MNRAS, 516, 1072
Di Carlo U. N., Mapelli M., Bouffanais Y., Giacobbo N., Santoliquido F., Bressan A., Spera M., Haardt F., 2020a, MNRAS, 497, 1043

Di Carlo U. N. et al., 2020b, MNRAS, 498, 495
Evans M. et al., 2021, preprint (arXiv:2109.09882)
Fairhurst S., 2009, New J. Phys., 11, 123006
Fairhurst S., 2011, Class. Quantum Gravity, 28, 105021
Fairhurst S., Hoy C., Green R., Mills C., Usman S. A., 2023, Phys. Rev. D, 108, 082006
Farmer R., Renzo M., de Mink S. E., Fishbach M., Justham S., 2020, ApJ, 902, L36
Fishbach M., Holz D. E., 2020, ApJ, 904, L26
Fragione G., Loeb A., 2023, ApJ, 944, 81
Gerosa D., Fishbach M., 2021, Nat. Astron., 5, 749
Graziani L., Schneider R., Marassi S., Del Pozzo W., Mapelli M., Giacobbo N., 2020, MNRAS, 495, L81
Green R., Hoy C., Fairhurst S., Hannam M., Pannarale F., Thomas C., 2021, Phys. Rev. D, 103, 124023
Hannam M., Brown D. A., Fairhurst S., Fryer C. L., Harry I. W., 2013, ApJ, 766, L14
Hijikawa K., Tanikawa A., Kinugawa T., Yoshida T., Umeda H., 2021, MNRAS, 505, L69
Inayoshi K., Visbal E., Haiman Z., 2020, ARA&A, 58, 27
Kalogera V. et al., 2019, BAAS, 51, 242
Klessen R. S., Glover S. C. O., 2023, ARA&A, 61, 65
Kremer K. et al., 2020, ApJ, 903, 45
Liu B., Bromm V., 2020, ApJ, 903, L40
Madau P., Haardt F., Dotti M., 2014, ApJ, 784, L38
Maggiore M. et al., 2020, J. Cosmol. Astropart. Phys., 2020, 050
Maiolino R. et al., 2023, preprint (arXiv:2308.01230)
Mancarella M., Iacovelli F., Gerosa D., 2023, Phys. Rev. D, 107, L101302
Mandel I., Farmer A., 2022, Phys. Rep., 955, 1
Mangiagli A., Bonetti M., Sesana A., Colpi M., 2019, ApJ, 883, L27
Mapelli M., Springer Singapore 2021, in Handbook of Gravitational Wave Astronomy. p. 16
Mapelli M., Bouffanais Y., Santoliquido F., Arca Sedda M., Artale M. C., 2022, MNRAS, 511, 5797
Marchant P., Moriya T. J., 2020, A&A, 640, L18
Mehta A. K., Olsen S., Wadekar D., Roulet J., Venumadhav T., Mushkin J., Zackay B., Zaldarriaga M., 2023, preprint (arXiv:2311.06061)
Mills C., Fairhurst S., 2021, Phys. Rev. D, 103, 024042
Mills C., Tiwari V., Fairhurst S., 2018, Phys. Rev. D, 97, 104064
Ng K. K. Y. et al., 2022, ApJ, 931, L12
Ng K. K. Y. et al., 2023, Phys. Rev. D, 107, 024041
Nitz A. H., Capano C. D., 2021, ApJ, 907, L9
Nitz A. H., Kumar S., Wang Y.-F., Kastha S., Wu S., Schäfer M., Dhurkunde R., Capano C. D., 2023, ApJ, 946, 59
Pezzulli E., Valiante R., Schneider R., 2016, MNRAS, 458, 3047
Pratten G. et al., 2021, Phys. Rev. D, 103, 104056
Punturo M., Lück H., Beker M., 2014, in Bassan M., ed., Astrophysics and Space Science Library, Vol. 404, Advanced Interferometers and the Search for Gravitational Waves, Springer-Verlag, Berlin, p. 333
Renzo M., Cantiello M., Metzger B. D., Jiang Y. F., 2020, ApJ, 904, L13
Ricarte A., Natarajan P., 2018, MNRAS, 481, 3278
Rodriguez C. L., Zevin M., Amaro-Seoane P., Chatterjee S., Kremer K., Rasio F. A., Ye C. S., 2019, Phys. Rev. D, 100, 043027
Roupas Z., Kazanas D., 2019, A&A, 632, L8
Safarzadeh M., Haiman Z., 2020, ApJ, 903, L21
Santoliquido F., Mapelli M., Iorio G., Costa G., Glover S. C. O., Hartwig T., Klessen R. S., Merli L., 2023, MNRAS, 524, 307
Schneider R., Valiante R., Trinca A., Graziani L., Volonteri M., Maiolino R., 2023, MNRAS, 526, 3250
Singer L. P. et al., 2014, ApJ, 795, 105
Spera M., Mapelli M., 2017, MNRAS, 470, 4739
Stacy A., Bromm V., 2013, MNRAS, 433, 1094
Stone N. C., Küpper A. H. W., Ostriker J. P., 2017, MNRAS, 467, 4180
Sugimura K., Matsumoto T., Hosokawa T., Hirano S., Omukai K., 2023, ApJ, 959, 17
Tanikawa A., Kinugawa T., Yoshida T., Hijikawa K., Umeda H., 2021, MNRAS, 505, 2170
Trinca A., Schneider R., Maiolino R., Valiante R., Graziani L., Volonteri M., 2023, MNRAS, 519, 4753
Usman S. A., Mills J. C., Fairhurst S., 2019, ApJ., 877, 82
Valiante R., Agarwal B., Habouzit M., Pezzulli E., 2017, Publ. Astron. Soc. Aust., 34, e031
Valiante R. et al., 2021, MNRAS, 500, 4095
van Son L. A. C. et al., 2020, ApJ, 897, 100
Veitch J. et al., 2015, Phys. Rev. D, D91, 042003
Vink J. S., Higgins E. R., Sander A. A. C., Sabhahit G. N., 2021, MNRAS, 504, 146
Vitale S., 2016, Phys. Rev. D, 94, 121501
Volonteri M., Rees M. J., 2005, ApJ, 633, 624
Volonteri M., Silk J., Dubus G., 2015, ApJ, 804, 148
Volonteri M., Habouzit M., Colpi M., 2021, Nat. Rev. Phys., 3, 732
Wadekar D., Roulet J., Venumadhav T., Mehta A. K., Zackay B., Mushkin J., Olsen S., Zaldarriaga M., 2023, preprint (arXiv:2312.06631)
Woosley S. E., Heger A., 2021, ApJ, 912, L31

APPENDIX A: DETECTOR SENSITIVITY

In this appendix, we show the sensitivity of ET and CE to binary mergers as a function of mass and redshift. Fig. 4 shows the sensitivity to mergers with mass ratio 2. In Fig. A1 we show the ET sensitivity for binaries with mass ratios 1, 2, 4, and 10. In Fig. A2, we show the same for CE. The maximum reach of the detectors is for equal-mass binaries. However, at equal mass the (3, 3) multipole vanishes so there is a larger range for which only one multipole is visible. As we increase the mass ratio, the maximum sensitive redshift decreases, as the amplitude of the emitted GW also decreases. However, the relative significance of the HoMs increases so that an increasing fraction of sources will be observed with at least two multipoles.

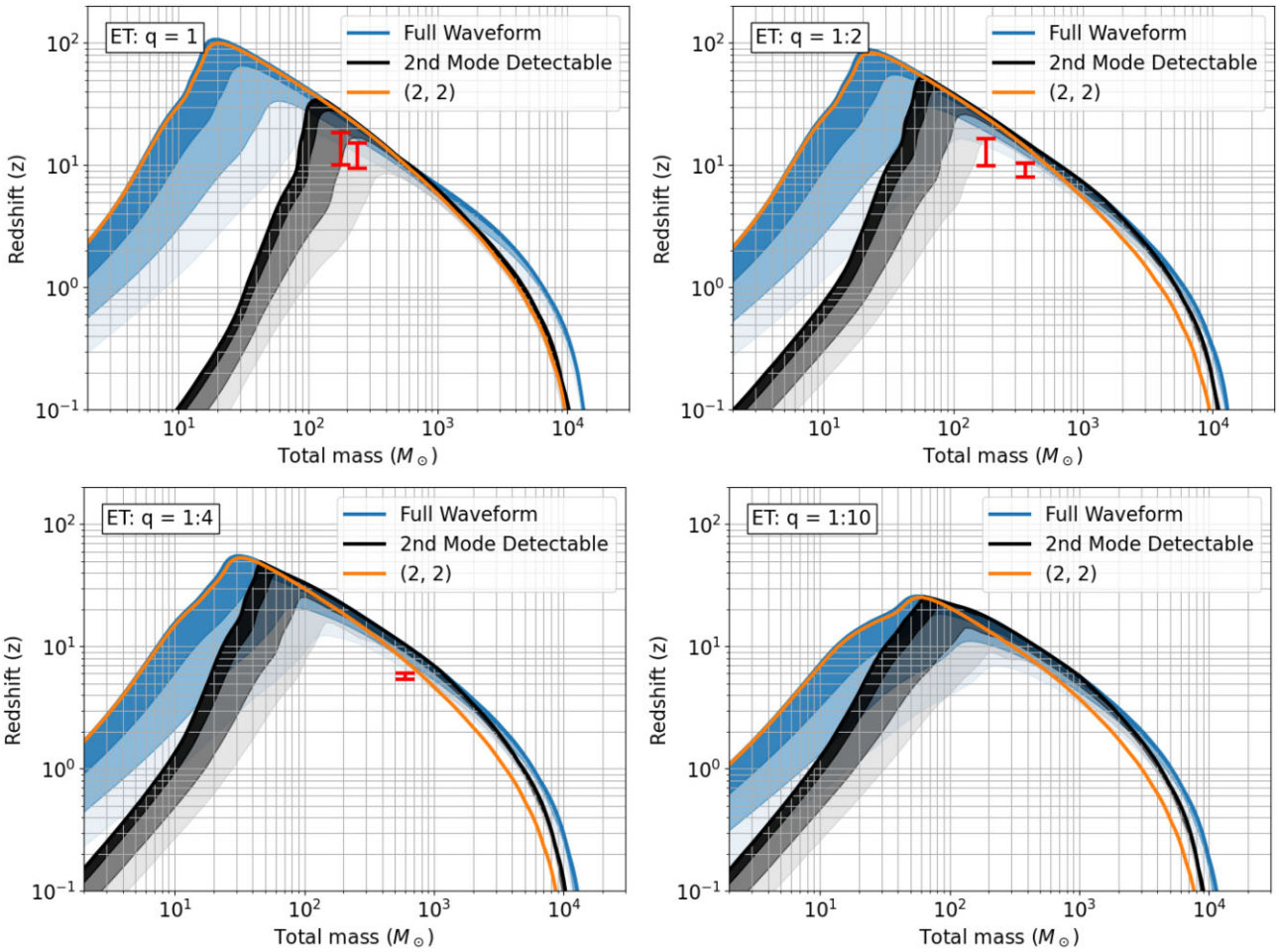

Figure A1. Maximum observable redshift of BBH mergers with ET for mass ratios $q = 1$, 1/2, 1/4, and 1/10. The shaded regions show redshifts at which 10 per cent, 50 per cent, and 90 per cent of sources are observable. The maximum observable redshift of the (2, 2) multipole at SNR = 8 is shown in orange, the observability of the full waveform at SNR = 8 is shown in blue, and the observability of the second most significant mode above SNR = 3 is shown in black. The red bars represent the masses and redshifts of the systems we study in detail in Section 3.

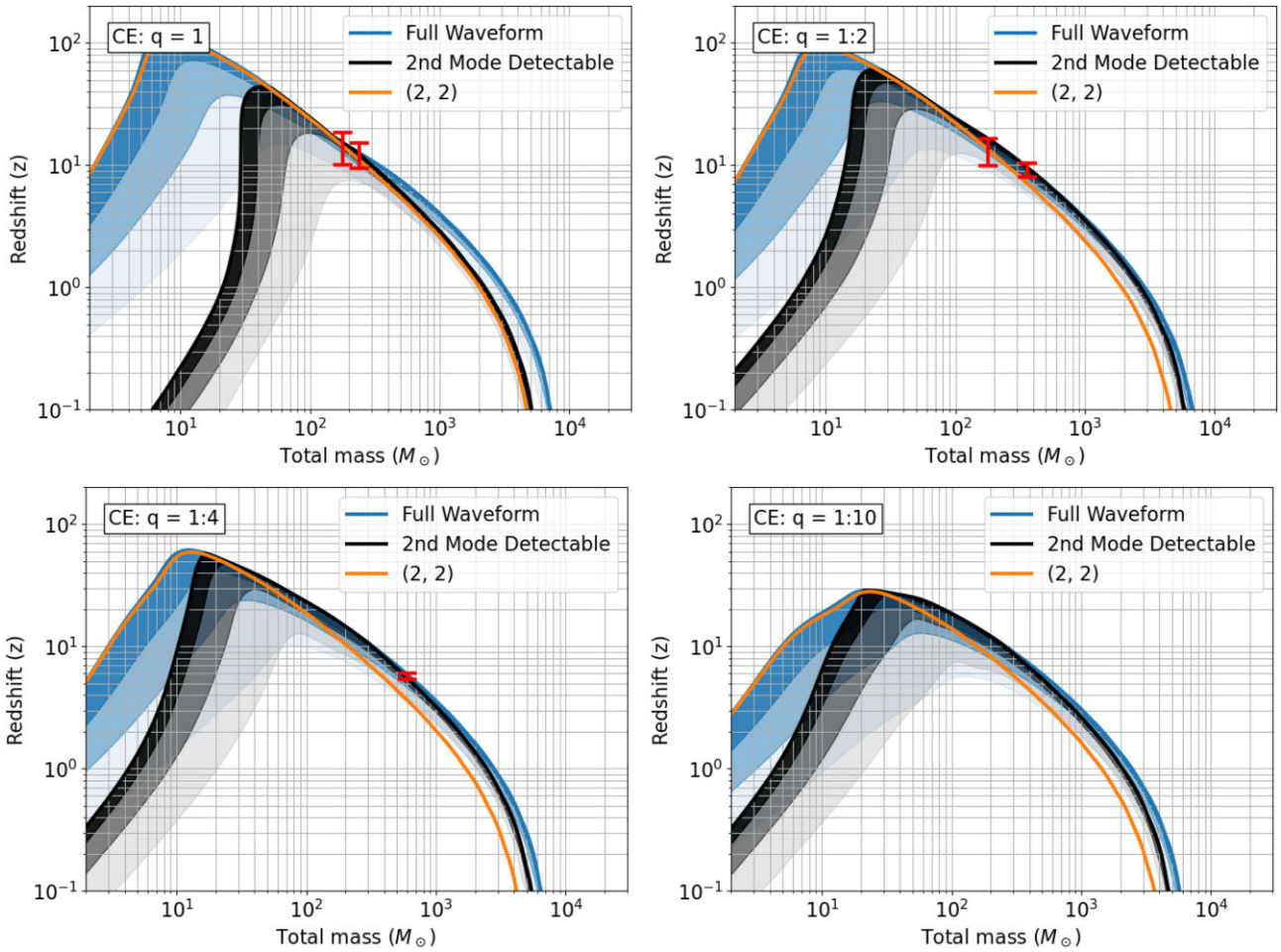

Figure A2. Same as A1 but for CE.

APPENDIX B: LOW SNR SIGNALS

In this appendix we present parameter estimation results for systems that would have a network SNR of 15 in the ET–CE network described in Section 3, to complement the results for SNR 30 presented in that section of the paper. Since these events are at a lower SNR, they are also at a higher redshift, with the $(120, 60)\,\mathrm{M}_\odot$ and $(90, 90)\,\mathrm{M}_\odot$ binaries at redshifts between 23 and 15 (depending upon inclination). At these redshifts, the signal is shifted to such low frequencies that it lies essentially outside of the sensitive band of CE – the SNR of these events in CE is less than 2 in all cases. Consequently, all sources are poorly localized on the sky, with a typical 90 per cent localization of thousands of square degrees.

In Figs B1 and B2, we show the accuracy with which the masses and redshift are recovered for the $(120, 60)\,\mathrm{M}_\odot$ and $(90, 90)\,\mathrm{M}_\odot$ binaries. The qualitative results are similar to those for the SNR 30 signals presented in Section 3, with broader posteriors as expected due to the lower SNR. Specifically, the masses and redshifts are poorly measured for face-on systems, and measurement accuracy improves for inclined systems (particularly $\iota = 60^\circ, 90^\circ$) where there is observable power in the HoMs. In the best-case scenarios, masses and redshifts are measured with ~ 25 per cent accuracy. For all systems other than $\iota = 0^\circ$ the $(120, 60)\,\mathrm{M}_\odot$ system is clearly identified as having unequal masses. However, the mass distributions are broad enough that limited information about the location of the pair-instability mass gap can be extracted.

For the $\iota = 0^\circ$ systems, and $\iota = 30^\circ$ for the $(90, 90)\,\mathrm{M}_\odot$ binary, there is a bimodality in the recovered redshift. In addition, the inferred mass distribution is broader than that shown in Fig. B1 and extends to $\sim 1000\,\mathrm{M}_\odot$. For these events, there is zero (or limited) power in the HoMs so only a single GW multipole is observable. The secondary peak at high masses and $z \approx 5$ corresponds to a binary configuration where the (3, 3) multipole has the correct amplitude and frequency content to match the simulated signal. This is discussed in more detail in Section 3, around Fig. 8.

In Figs B3 and B4, we show the accuracy with which the masses and redshift are recovered for the $(240, 120)\,\mathrm{M}_\odot$ and $(480, 120)\,\mathrm{M}_\odot$ binaries. As for the lower mass systems, the qualitative results are similar to those for the SNR 30 signals presented in Section 3, with broader posteriors as expected due to the lower SNR. None the less, other than the face-on ($\iota = 0^\circ$) systems, the binaries are clearly identified as unequal-mass systems containing an IMBH with

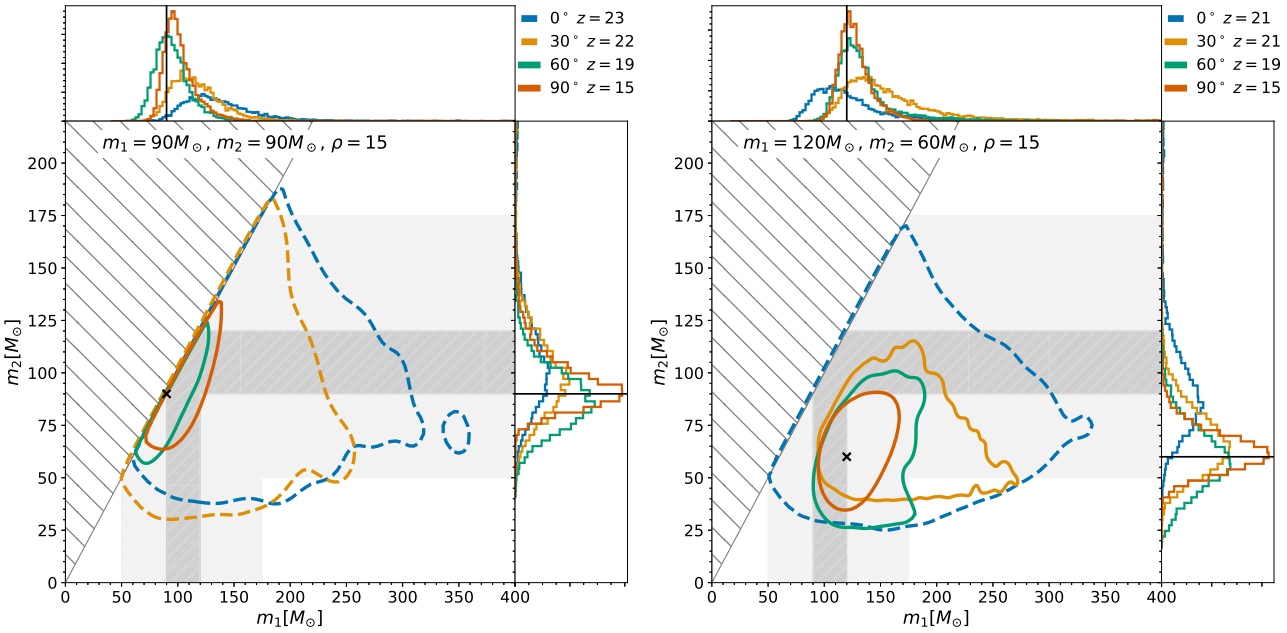

Figure B1. Inferred posteriors of component masses for binaries of total mass of 180 $M_\odot$ which straddle, or sit within the upper mass gap. Results are shown for inclinations of $\iota = 0°$, 30°, 60°, and 90°, with the redshift of the system varied, as indicated in the labels, so that the signals are all simulated with an SNR of 15 in the ET–CE network, at the most sensitive sky location for the network. The grey region denotes the mass gap, whose location varies with the $^{12}C(\alpha, \gamma)^{16}O$ reaction rate, and the darker grey denotes the forbidden strip (Farmer et al. 2020). Simulated values are denoted by a black cross and contours show the 90 per cent credible region. Left: Binary with masses just below the mass gap: $m_1 = m_2 = 90\,M_\odot$. Right: Binary with masses that straddle the mass gap: $m_1 = 120\,M_\odot$ and $m_2 = 60\,M_\odot$.

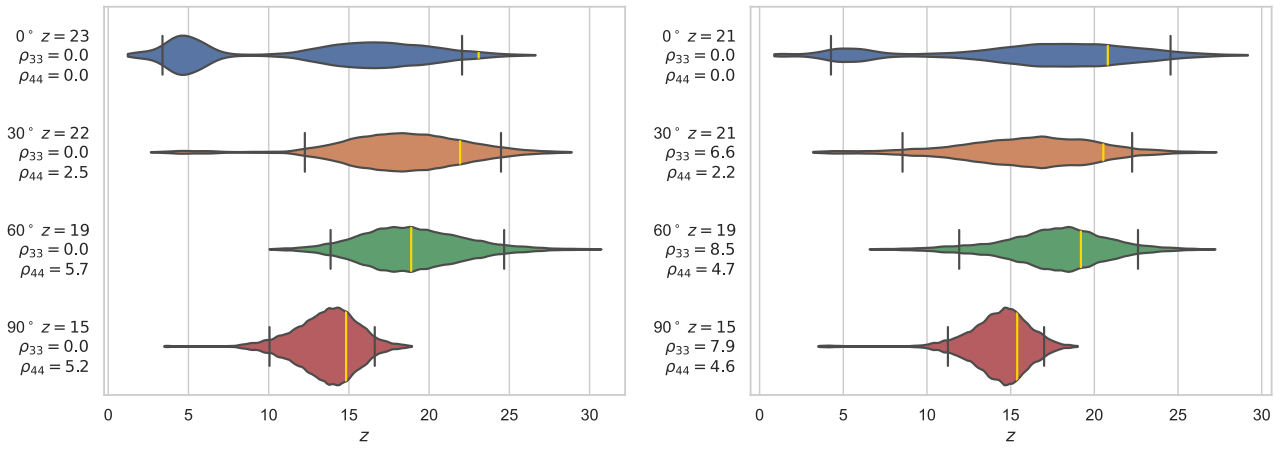

Figure B2. Inferred posteriors for the redshift for binaries of total mass of 180 $M_\odot$ which straddle, or sit within the upper mass gap. Signals are simulated with varying inclination and redshift, as indicated in the labels, with a fixed SNR of 15 in the ET–CE network, at the most sensitive sky location for the network. The vertical lines indicate the 90 per cent credible intervals, violins show the 99.5 per cent range, and the yellow vertical lines show simulated values. Symbols $\rho_{\ell m}$ indicate the SNR in the (ℓ, m) multipole HoMs. Left: Binary with masses just below the mass gap: $m_1 = m_2 = 90\,M_\odot$. Right: Binary with masses that straddle the mass gap: $m_1 = 120\,M_\odot$ and $m_2 = 60\,M_\odot$.

minimum mass 200 $M_\odot$/400 $M_\odot$ for the two system. Redshifts are generally underestimated, likely due to the poor sky localization, and lower bounds on the redshift are *no better* than for the higher SNR systems shown in Fig. 10.

Again, the face-on systems show significant bimodality with a second peak at much lower redshifts and higher masses. As before, this corresponds to a system where the HoMs, rather that the (2, 2) multipole, are associated with the observed waveform.

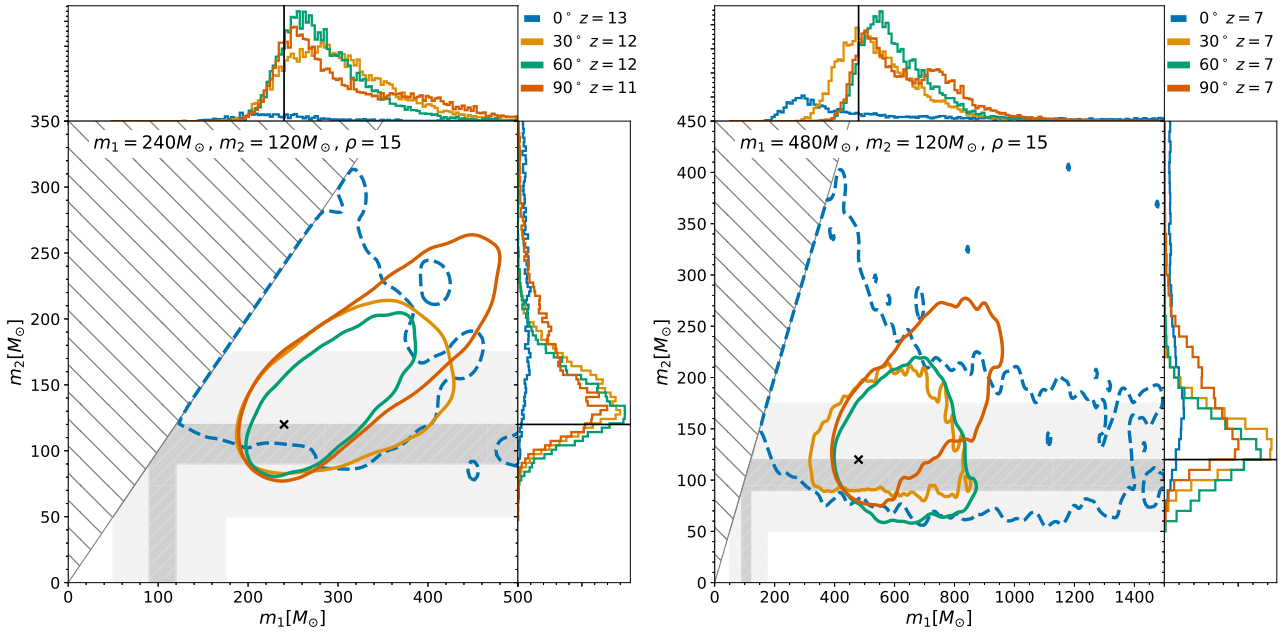

Figure B3. Inferred posteriors for the component masses for heavy binaries. Results are shown for inclinations of $\iota = 0°$, $30°$, $60°$, and $90°$, with the redshift of the system varied, as indicated in the labels, so that the signals are all simulated with an SNR of 15 in the ET–CE network, at the most sensitive sky location for the network. The grey region denotes the pair-instability mass gap and the darker grey denotes the forbidden strip where no BH is expected to form for any value of the $^{12}C(\alpha, \gamma)^{16}O$ reaction rate (Farmer et al. 2020). Simulated values are denoted by a black cross and contours show the 90 per cent credible region. Left: $m_1 = 240\,M_\odot$ and $m_2 = 120\,M_\odot$. Right: $m_1 = 480\,M_\odot$ and $m_2 = 120\,M_\odot$.

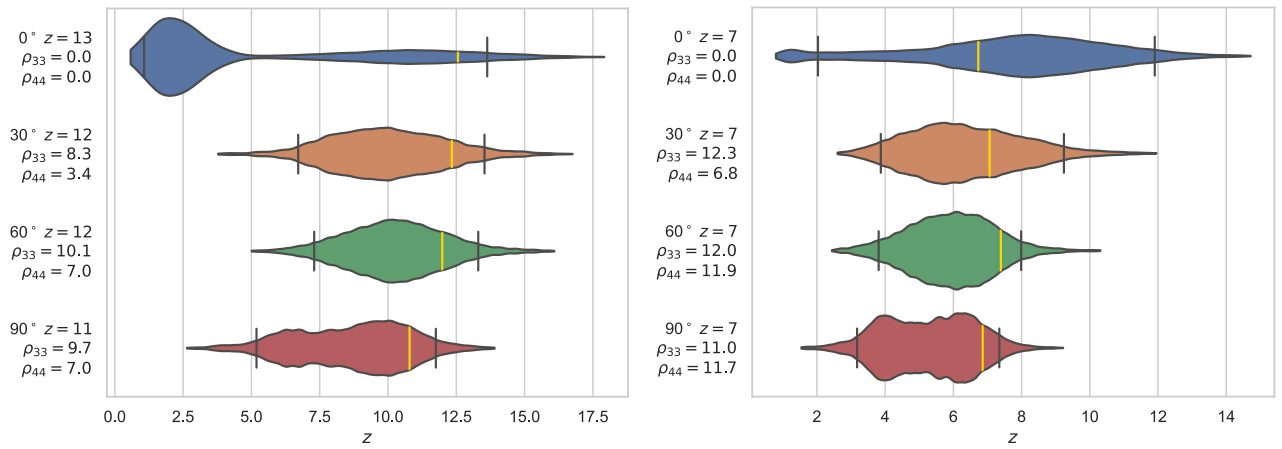

Figure B4. Inferred posteriors for the redshift for heavy binaries. Signals are simulated with varying inclination and redshift, as indicated in the labels, with a fixed SNR of 15 in the ET–CE network, at the most sensitive sky location for the network. The black vertical lines indicate the 90 per cent credible intervals, violins show the 99.5 per cent range, and the yellow vertical lines show simulated values. Symbols $\rho_{\ell m}$ indicate the SNR in the (ℓ, m) multipole HoMs. Left: $m_1 = 240\,M_\odot$ and $m_2 = 120\,M_\odot$. Right: $m_1 = 480\,M_\odot$ and $m_2 = 120\,M_\odot$.

This paper has been typeset from a TEX/LATEX file prepared by the author.